Scientific Research

Topology-Optimized Segmental 3D-Printed Concrete Footbridge Activated by Post-Tensioning: Design, Manufacturing and Assembly Demonstration

Albert de la Fuente [1], Eduardo Galeote [2], Alejandro Nogales [1], Ye Xia [3], Fangyuan Li [3,*]

[1] Dept. of Civil and Environment Engineering, Universitat Politècnica de Catalunya (UPC), BarcelonaTech. C// Jordi Girona 1-3, 08034, Barcelona, Spain;
[2] Dept. of Architectural Technology, Universitat Politècnica de Catalunya (UPC), BarcelonaTech. Av. Dr. Marañón 44-50, 08028, Barcelona, Spain;
[3] Department of Bridge Engineering, Tongji University, Shanghai 200092, China.
* Correspondence: fyli@tongji.edu.cn

Abstract: This paper presents Goliath footbridge, a full-scale 6 m span segmental 3D-printed concrete footbridge activated by post-tensioning, describing the end-to-end process from design and fabrication to transport, assembly, and structural activation. This structure represents the demonstrator of a research project that was conceived as an end-to-end demonstrator integrating material development, digital design, additive manufacturing, and site erection. The printable mortar was previously characterized through rheological and mechanical tests to verify extrusion performance, buildability, and strength development. The structural geometry was obtained through topology optimization under self-weight and pedestrian service loads, aiming to maximize stiffness and reducing material consumption. The resulting solution provided an efficient lightweight configuration adapted to additive manufacturing. After production, the segments were transported to site, rotated into their final position, assembled on temporary supports, aligned through the dry-joint system, and sequentially activated by post-tensioning. The demonstrator confirmed the technical feasibility of combining topology optimization, modular 3D concrete printing, dry-joint assembly, and post-tensioning for pedestrian bridge applications. It also highlighted practical challenges related to dimensional tolerances, local stress concentrations, cracking sensitivity, and durability of joints and anchorage zones. The study provides a practical proof of concept for future scalable 3D-printed concrete bridge construction.

Keywords: topology-optimized; 3D-print; concrete footbridge; post-tensioning

Citation: da la Fuente, A.; Galeote, E.; Nogales, A.; Xia, Y.; Li, F. Topology-Optimized Segmental 3D-Printed Concrete Footbridge Activated by Post-Tensioning: Design, Manufacturing and Assembly Demonstration. *Prestress Technology* **2026**, *2*, 01-21. https://doi.org/10.59238/j.pt.20260429001

Received: 29/04/2026
Accepted: 29/05/2026
Published: 25/06/2026

Publisher's Note: Prestress technology stays neutral with regard to jurisdictional claims in published maps and institutional affiliations.

1 Introduction

Digitization and automation are currently gaining significant relevance in the construction industry. In this context, the use of 3D-printed concrete (3DPC) has generated growing interest in architectural and engineering environments given the advantages in freedom of complex geometries and reduction of construction times, labour and material costs [1]. Proof of this are the numerous works conducted with 3D printing technology [2,3], which have also demonstrated beneficial environmental and social impact in comparison to traditional solutions [4].

To achieve a greater impact of 3DPC in the construction sector, it becomes necessary to broaden the applications to more demanding structural elements. This transition requires establishing standardised production systems and quality control protocols to guarantee the mechanical performance of 3DPC. For this, the RILEM TC 303-PFC and 304-ADC published a collection of reports [5-9] focused on the mechanical and durability assessment of 3DPC properties aimed at providing a representative basis for standardised testing and future building codes.

Despite the efforts and advancements conducted, the implementation of 3DPC at a large-scale dimension still faces several bottlenecks. Among those, scalability represents a major challenge given the dimensional limitations of the 3D printers [10], hindering the production of single monolithic elements and making industrial production of 3D-printed elements move towards modular fabrication [11]. However, this approach also introduces the problem of transportation and structural continuity of the modular elements that require being connected to ensure a monolithic structural behaviour.

In this scenario, post-tensioning technology is seen as a suitable solution to provide structural continuity. In this approach, ducts or voids are designed to be left during printing, where tendons are inserted after curing and then tensioned to introduce compressive stresses that provide the required structural continuity and keep joints closed [12-15]. Unlike traditional rebars, whose use might be affected by their stiffness and consequent geometrical limitations, post-tensioning tendons could be able to adapt to non-straight voids without excessive curvatures [16].

The Goliath footbridge addresses these challenges describing the design, fabrication, and assembly. Based on an initial study of the rheological and mechanical properties of the material, a topological optimisation was conducted to structurally design the footbridge and define the requirements for its fabrication. As displayed in the design layout (Figure 1), the segmental design was necessary to overcome the abovementioned scalability issues, leading to a production of four modules connected through a system of dry joints and shear keys. During the assembly phase, the segments were placed on provisional supports. After assembly and alignment, a non-bonded post-tensioning system was used to ensure structural continuity and provide the footbridge a monolithic behaviour, installing permanent supports and removing the temporary ones.

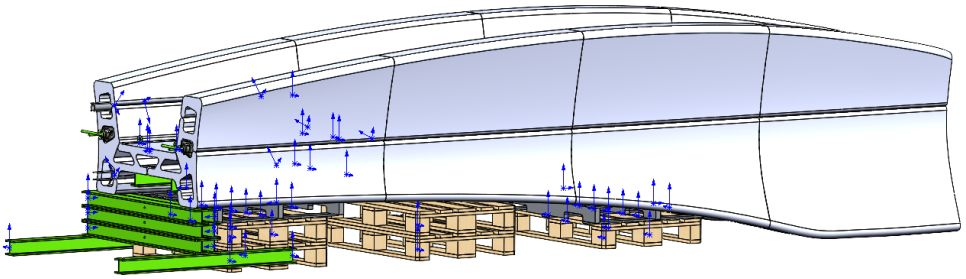

Figure 1 Design layout of the footbridge

This demonstrator exhibits an end-to-end validation of the full workflow from digital design to site-like erection. This work mainly focuses on the construction and structural viability and additional aspects such as long-term durability or dry-joint system behaviour were intentionally left for future works. In this regard, this work serves as a proof of concept, positioning itself as an integrated demonstration of a 3D-printed, segmental footbridge activated by post-tensioning and providing valuable knowledge involving constructability and assembly.

2 3D-Printed Bridges/Footbridges and Continuity Strategies

2.1 Overview of 3D Printed Concrete Bridges

In the last decade, several 3DPC bridges and footbridges for both pedestrian and cycling uses have been manufactured at full scale. These projects provide evidence on the feasibility, advantages, and limitations of 3DPC, considering different printing technologies. Table 1 summarises representative 3D printed bridges, presenting their main structural characteristics, materials, and construction technology, including reinforcement and continuity strategies showing the technological assembly evolution. The bridges listed present a variety of reinforcement concepts, showing

 https://doi.org/10.59238/j.pt.20260429001

the combination of 3DCP with different types of reinforcement adapted to different printing methods and geometries.

Table 1 Representative 3DPC bridge projects

Project		Type / Span	Location & Cons. Period	Material & Technology
a)		Ped. (12m)	Madrid, Spain (2014—2016) [17,18]	Micro-RC; Seg. Prin. Ass.
b)		Cyc. (8m)	Gemert, the Netherlands (2017) [15]	Concrete RSW; 6 Seg. Prin. Ass.
c)		Ped. (14.4 m)	Shanghai, China (2019) [19]	RC; 44 Seg. Prin. Ass.
d)		Ped. (17.9 m)	Tianjin, China (2019) [4]	FR-mortar; Seg. Prin. Ass. Post-tensioned bars
e)		Ped. (4 m)	Ghent, Belgium (2019) [20]	Grout mortar; 18 Seg. Prin. Ass. Post-tensioned

Project		Type / Span	Location & Cons. Period	Material & Technology
f)		Ped. (6 m)	Tokyo, Japan (2020) [21]	Concrete; 44 Seg. Prin. Ass. Post-tensioned
g)		Ped. / Cyc. (5 uts x 5.8 m)	Nijmegen, the Netherlands (2021) [22]	Concrete; 23 Seg. Prin. Ass. Post-tensioned
h)		Ped. (16 m)	Venice, Italy (2021) [23,24]	Concrete; 53 blocks
i)		Ped. / Cyc. (4.75 m)	Ghent, Belgium (2022) [25]	Concrete; Outer shell filled on site. Post-tensioned
j)		Cyc. (11 m)	N243 Route, the Netherlands (2022) [4]	Concrete; 6 Seg. Hollow-core Post-tensioned

Legend: Cons. period: construction period; **Ped.**: pedestrian; **Cyc.**: cyclist; **RC**: reinforced concrete; **Seg. Prin. Ass.**: segments printed and assembled; **RSW**: reinforced with steel wire during 3D printing.

Credit: a) Municipality of Alcobendas, b) Marc Zoutendijk, c) Tsinghua University, d) Xinhua, e) Vertico, f) Taiheiyo Cement, g) Michiel van der Kley, h) Naaro, i) University of Ghent, j) Saint-Gobain Weber.

https://doi.org/10.59238/j.pt.20260429001

The Parque de Castilla footbridge in Madrid [18,26] used the D-Shape technology [17] to produce eight fibre-reinforced cement-based segments exhibiting a U-shaped geometry. Once assembled, the footbridge reached a span of 12 m, supported by a curved steel frame which ensured global stability and guaranteed the load-bearing capacity in case of degradation of the printed material.

In subsequent bridges, produced by contour-printing, the printed segments are the primary load-bearing components. The Gemert cycling bridge [15] presents an 8 m span, and is composed of six printed segments, with a post-tensioning system providing structural continuity. Other bridges such as those constructed in Shanghai [19] and Tianjin [4] also used printed fibre-reinforced mortar segments. The footbridge in Shanghai consisted of a square-section arch composed by 44 segments, although additional 68 printed elements were used for the parapet and 64 for the pavement. For its construction, steel arch angles were installed as temporary supports during segments assembly before completion and self-supporting. This construction method contrasts with the Tianjin bridge, which used post-tensioned bars to connect printed segments.

Following a similar approach as in the Gemert bridge, the 3D printed girders in Ghent [20] were manufactured in 18 segments, including a post-tensioning system to provide structural continuity. The Tokyo 6 m pedestrian bridge [21] also used a similar post-tensioned method for assembling 44 concrete segments that included designed holes for rebar insertion after printing. Later, a multi-span bridge in Nijmegen [22] achieved approximately a length of 29 m, using post-tensioned segments and conventional concrete infill at critical regions.

The Striatus bridge in Venice [23,24] was based on 53 unreinforced alveolar segments of variable section and length printed using contour-printing techniques. It forms a 16 m span arch where stability derives almost entirely from compression geometry. Even though concrete presents load-bearing capacity, steel tie-bars installed at the supports collect horizontal loads.

Finally, the Ghent prototype [25] adopted an approach using 3D-printed outer shells segments filled with self-compacting concrete with two anchorage blocks for achieving a 4.75 m span. Finally, the N243 Route cycling bridges [4] in the Netherlands, presents a project consisting of four bicycle bridges composed by six post-tensioned segments leading to 11 m spans.

These projects represent the context from early proof-of-concept structures relying on external reinforcement or compression-only forms, towards increasingly demanding applications that combine segmental assembly, dry-joint systems, and post-tensioning to achieve structural continuity over longer spans. The GOLIATH footbridge presented in this paper advances this trajectory by integrating topology-optimised geometry, a tongue-and-groove dry-joint interlocking system, and post-tensioning activation within a digital end-to-end workflow that targeted the structural performance and constructability requirements that remain open challenges within this field.

2.2 Segmental Assembly of 3D Printed Elements

Despite the benefits of prefabrication and modularization, the experience from the existing modular prefabricated and 3D-printed constructions highlights several open challenges that need to be addressed so 3D-printed systems can be widely adopted. Although steel reinforcement integration in 3D printed concrete structures still represents a major challenge, issues specifically related to modular fabrication

such as tolerance management, shear transfer across joints, quality assurance, and repeatability also arise when producing and assembling segments.

Tolerance management becomes an issue of utmost importance given that minor print or assembly misalignments may generate issues regarding constructability, fit between components, structural stability, and safety [27-30], which leads to the necessity of conducting rigorous quality controls. Accordingly, prefabricated elements that are assembled on site require a proper fit ensuring the absence of excessive gaps between interfaces, since their presence may trigger stress concentrations that could jeopardise performance and structural safety [31,32].

Additional requirements for assembling prefabricated 3DPC segments are the development of mechanical interlocks, which provide structural integrity to the global assembly and contribute to avoiding slippage between segments. In this regard, the geometric design of segment connections is a critical factor in their performance. Previous studies have analysed various self-locking interface geometries [30,33-36], as well as the effectiveness of the shear key angles and the specific inclination of the shear joints [37].

To further enhance this mechanical interference and compensate for printing tolerances, some examples in the literature use wet-join solutions based on the use of mortar [1] to seal joints and gaps between segments for ensuring full contact. Other studies combine the insertion of steel rebars [38] or post-tensioning [15] with void grouting and the use of synthetic epoxy-based resin or mortar for bonding the segments and smoothen surfaces, thus improving load transfer across joints and avoiding local peak stresses. Conversely, and even though wet-joint configurations usually present a greater shear strength than dry-joints [39-41], the latter have also been investigated by different researchers given their simplicity, speed of assembly and structural stability [42,43].

The full industrialization of modular 3D printed construction also requires ensuring geometric accuracy and repeatability. As a result of the lack of formwork, 3DPC may present cumulative errors that might lead to collapse [44]. This requires advanced quality control techniques such as AI-assisted computer vision to quantify defects and layer dimensions in real time [45] to achieve and guarantee repeatability and dimensional tolerances despite the variabilities in material rheology, printing parameters or layer and elements dimension [46].

3 Integrated Design: Material and Structure

3.1 Material Design for 3D Printing

The dry fraction of the 3D printing mortar mix was produced with Portland cement CEM I and fine aggregates of maximum grain size of 2 mm. The cement content was set at 25% with a water content of 20%, this adjusted to achieve the desired balance between shear fluidity and stability during the printing process. Additionally, standard additives were incorporated to adjust the flowability, workability and printability.

The rheological characterization of the mortar was conducted through rotational tests using an Anton Paar MCR 102e rheometer, equipped with the BMC90 module specifically designed for high-concentration cementitious pastes and mortars. The tests were performed by applying controlled shear rate stresses for the obtention of flow curves and the analysis of the structural cohesion and the apparent viscosity evolution as a function of the shear rate, as shown in the results displayed in Figure 2 a) and b). This procedure was conducted at time intervals of 15, 30 and 45 minutes after the mortar preparation to evaluate the influence of setting time on the rheological behaviour during the early stages of the material production.

 https://doi.org/10.59238/j.pt.20260429001

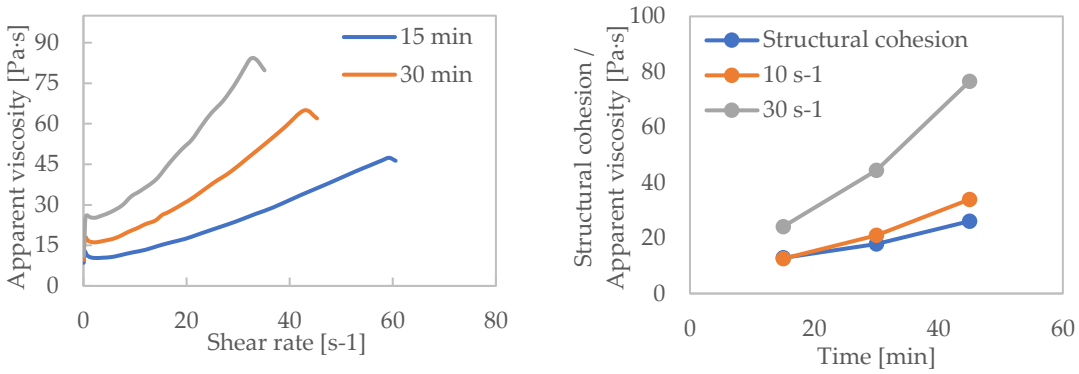

a) Apparent viscosity b) Structural cohesion / Apparent viscosity

Figure 2 Structural cohesion and apparent viscosity as a function of shear rate after mortar preparation (15, 30, and 45 min)

The results show a progressive increase in apparent viscosity as the shear rate increases, this exhibiting a non-Newtonian and pseudoplastic behaviour. This behaviour remained consistent across all analysed time intervals. Additionally, a progressive increase in apparent viscosity is observed over time following the preparation of the mortar, which could be attributed to the initial structuring and setting processes of the mortar.

From the perspective of additive manufacturing with cementitious materials, the observed rheological behaviour is particularly suitable as the structural cohesion ensures geometric stability after deposition and apparent viscosity remains within the operational printing and extrusion time window. The material shows a temporal evolution of viscosity, highlighting the existence of a workability window compatible with manufacturing times, allowing for a controlled extrusion of the material due to an increase of consistency with age, favouring geometric stability after deposition without premature loss of fluidity or structural collapse.

The mechanical characterization of the material was conducted through compressive tests on cylindrical specimens ⌀150x300mm according with UNE-EN 12390-3 [47] at different curing times to analyse the evolution of the mechanical properties of the materials. Figure 3 shows the average results of the compressive strength, exhibiting a progressive increase in performance over the curing period, reaching 19.3 MPa at 28 days. This evolution is consistent with the expected behaviour of a cementitious mortar formulated for additive manufacturing processes, where early-age strength is required to ensure geometric stability without compromising initial workability.

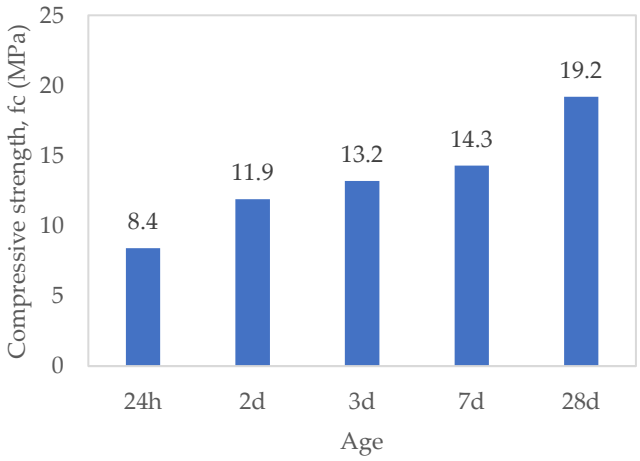

Figure 3 Compressive strength of the mortar at different curing times (cylindrical specimens)

Flexural tests were also conducted on prismatic specimens 160x40x40mm following the specifications of the standard UNE-EN 196-1:2018, with both halves of the specimens tested for determining the flexural strength subsequently used to obtain and verify additional compressive strength data (Figure 4). Flexural strength exhibited values of 3.0 MPa at 7 days and 5.8 MPa at 28 days, confirming an adequate load-bearing capacity under flexural stress. This performance is relevant both for the handling and assembly phases and for the long-term service behaviour of the printed elements. Compressive strength exhibited values of 14.6 MPa at 7 days and 17.8 MPa at 28 days.

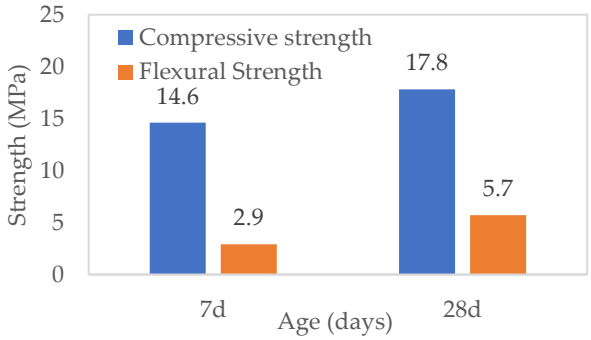

Figure 4 Compressive and flexural strength of the mortar at different curing times (prismatic specimens)

3.1.1 Optimisation Algorithm and Strategy

The structural topology optimization was conducted using the TOSCA engine within the Abaqus/CAE [48] environment. Unlike gradient-based methods often used in density-based optimization, this study resorts to the robust integration of Finite Element Analysis (FEA) with an automated optimization workflow, ensuring data transfer between the generative phase and the subsequent 3D design stages.

The optimization process is governed by a Genetic Algorithm (GA), a metaheuristic approach based on the principles of natural selection and evolutionary biology [49]. In this framework, a population of potential topological solutions evolves through stochastic operators to maximize the fitness function. This global search capability is particularly advantageous for the current study as it handles the non-linearities inherent in structural connectivity and allows for the exploration of a broad design space without the requirement of sensitivity derivatives.

The optimization approach focused exclusively on Topology Optimization. This method aims to define the optimal material distribution within a predefined design domain by modifying the relative density and stiffness of the individual finite elements.

The optimization problem was formulated to find the design with maximum global stiffness (minimum compliance) under a volume fraction constraint. The general mathematical structure of the objective function and constraints can be expressed as:

- Objective Function: Minimization of the Strain Energy, which serves as a proxy for maximizing structural stiffness under the prescribed loading conditions.
- Design Constraints: A target volume reduction (or weight limit) was imposed to ensure material efficiency while satisfying boundary conditions and internal stress and deflection limits.

The optimization starts from an initial solid domain representing the maximum allowable geometric envelope of the footbridge. Through iterative cycles, the algorithm re-evaluates the contribution of each element to the overall structural integrity. Elements with low strain energy density are progressively penalized or removed, effectively sculpting the optimal load-bearing path. This process continues until the convergence criteria are met, yielding a biomimetic-like geometry that represents the most efficient distribution of concrete for the bi-supported span.

https://doi.org/10.59238/j.pt.20260429001

3.1.2 Design of the Footbridge

Based on the comparative analysis of the topological iterations, a final design was selected for experimental validation, representing the optimal balance between structural stiffness, material efficiency, and constructive feasibility. The optimization process started from a solid domain representing the maximum allowable geometric envelope of the footbridge, as illustrated in Figure 5. The deck of the footbridge not included in the domain to be optimised, set as a restriction. It should be noted that, due to the structural and loading symmetry of the problem, only a half of the domain was modelled (symmetry with respect to the longitudinal plane), allowing for a less computation cost and runtime.

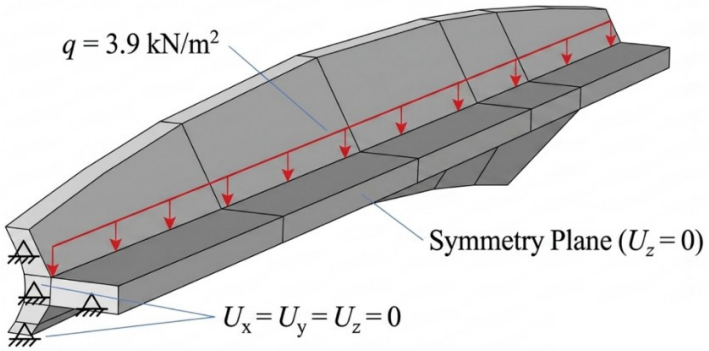

Figure 5 Original domain for the topology optimisation analysis (boundary and load conditions)

The topological optimisation of the geometry was done subjected to its self-weight and a uniformly distributed service load of 3.9 kN/m², the latter consistent with a common design load for footbridges, prioritizing the minimization of strain energy to ensure a stable stress distribution. In terms of structural performance, the solution was required to maintain a strictly controlled vertical displacement, with a maximum allowable deflection of 3.30 mm. Furthermore, the optimization was governed by a stress limit, ensuring that maximum tensile stresses remained below 2.50 MPa during the generative phase. This being a common value for concrete tensile value. The resulting geometry achieves a significant mass reduction, in this regard it was requested a volume fraction of approximately 50% of the original design domain without compromising serviceability requirements.

The resulting geometry from the topology optimization analysis, depicted in Figure 6, effectively sculpts the structure by removing the majority of the material volume from the beam webs in the vicinity of the mid-span. In this central region, flexural forces are predominant over shear forces; consequently, the material is strategically concentrated at the top and bottom flanges to withstand the high normal forces, acting in either tension or compression.

On the contrary, towards the supports, the optimization logic shifts to address the predominance of shear forces. In these areas, more material volume is retained at the web of the beam to provide shear resistance, while it is progressively removed from the top and bottom flanges. Regarding the overall mechanical behaviour, the resulting geometry bears a strong resemblance to an arch-like system, where the load is supported through an optimized distribution of struts and ties.

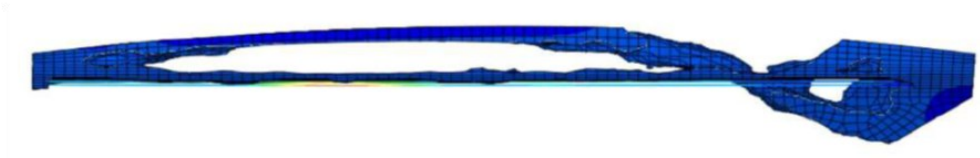

Figure 6 Resulting geometry after conducting the topology optimisation analysis

It is important to emphasize that this optimized geometry is highly dependent on the specific loading and boundary conditions prescribed. The current distribution represents the most efficient load-bearing path for the distributed service load, however, different topological configurations emerged under alternative scenarios, such as point loads. This arch-like behaviour is particularly advantageous for the project's objectives, as it aligns the internal compression paths with the 3D-printed concrete's strengths and allows identifying the precise trajectories where the post-tensioning system is required to bridge the segments and ensure monolithic structural action.

3.2. Manufacturing Design

3.2.1 Design of the Segments

The designed footbridge was developed integrating an optimized internal geometry developed through the optimized structural generative design previously described combined with a post-tensioning system. Due to manufacturing and logistical limitations, the structure was designed as a modular system consisting of four 3D-printed concrete segments (Figure 7), with a total length of 6 meters. The full design of the footbridge consists of four hollow segments (each with a mass ranging from 1.08 to 1.29 tones), with a total structure mass of approximately 4.8 tones.

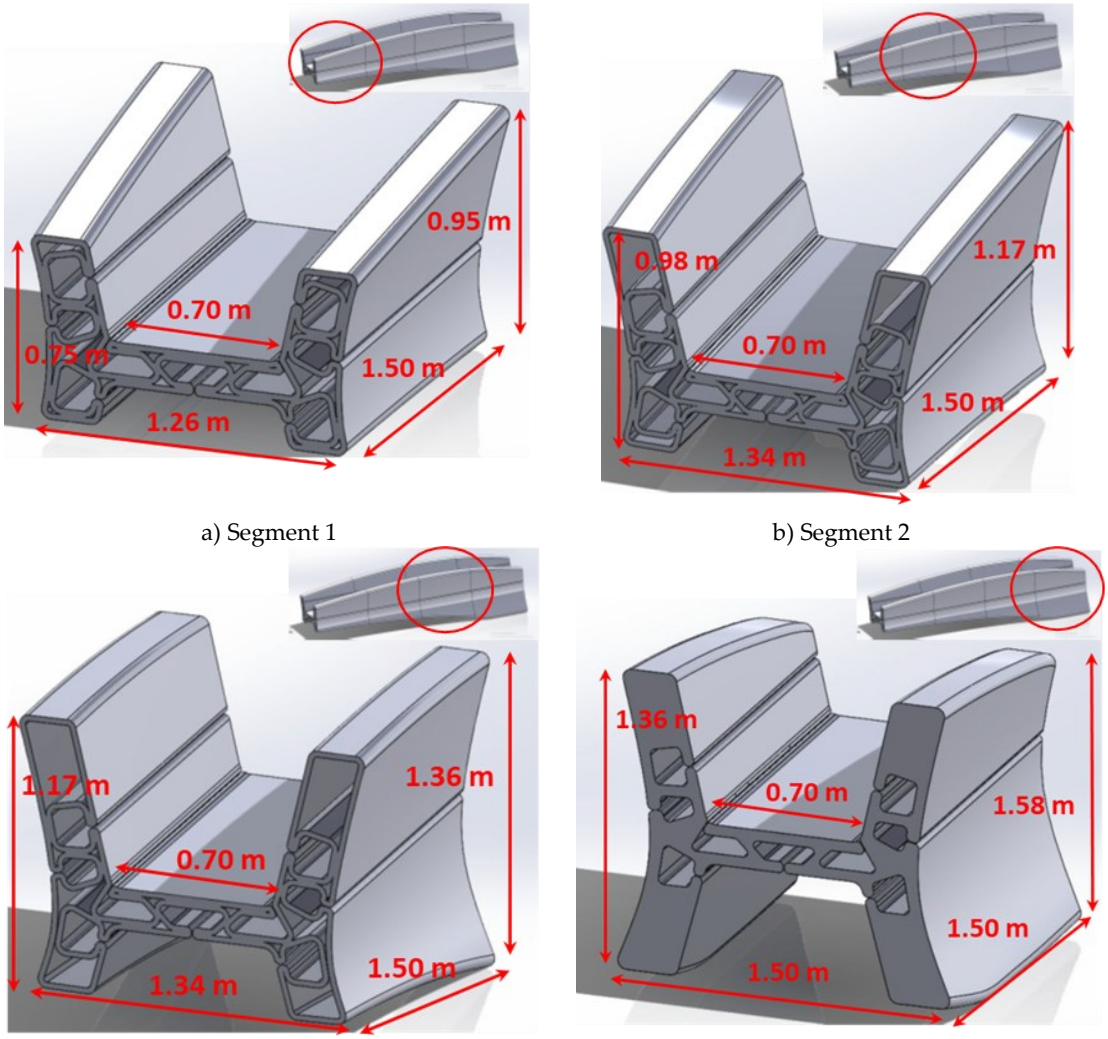

a) Segment 1 b) Segment 2

c) Segment 3 d) Segment 4

Figure 7 Schematic representation and dimensions of the segments

The structural integrity was validated through linear static finite elements analysis conducted in SolidWorks Simulation®. The concrete was modelled as a

 https://doi.org/10.59238/j.pt.20260429001

linear elastic isotropic solid, with an elastic modulus E of 28.3 GPa, Poisson coefficient ν = 0.2 and density ρ = 2400 kg/m^3. The boundary conditions consisted of a fixed support at one end and a vertical roller at the opposite. Loading parameters included gravitational loads, two service loads incorporated as distributed normal forces of 1.52 kN on the deck, and progressive axial forces at the anchorages ranging from 100 kN to 800 kN to simulate different post-tensioning levels at the post-tensioned tendons. For the simulation, the computational model was developed using a solid mesh with 158,000 high-order quadratic elements (16-point Jacobian) and approximately 300,000 nodes, with element sizes varying between 50 and 200 mm.

3.2.2 Detailing for Post-Tensioning and Joints

The connection between the 3D-printed concrete segments is based on a dry joint system, using a polymeric interlocking tongue-and-groove geometry integrated directly into the segment faces to ensure the alignment of the modules during placement. Additionally, and given that the elements were printed in four separate segments and lacked traditional reinforcement, a post-tensioning system was designed to produce a monolithic element by compressing the segments and ensuring that the joints remain closed and capable of transferring shear forces through friction and mechanical interlock. Figure 8 shows the final design of the footbridge, indicating the position of both the tongue-and-groove system and the post-tensioning elements.

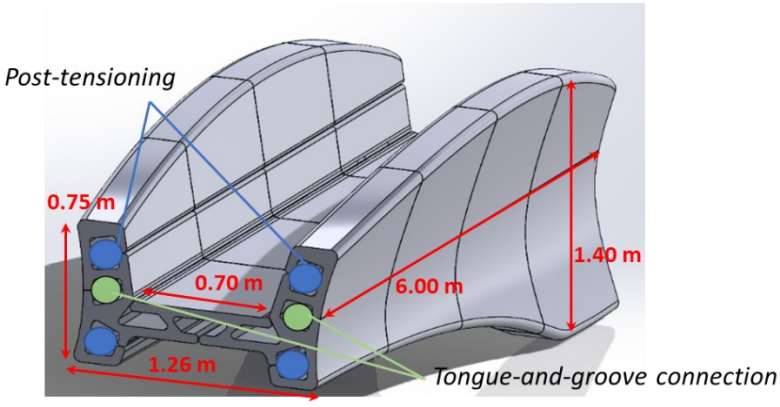

Figure 8 Final design of the footbridge

For the tongue-and-groove connection, polymeric inserts were designed in both protrusion and recess configurations to facilitate and ensure alignment during assembly of the segments, as well as effectively transfer shear stresses between elements without wet-joint solution. Figure 9 shows a representation of both elements, along with its dimensions.

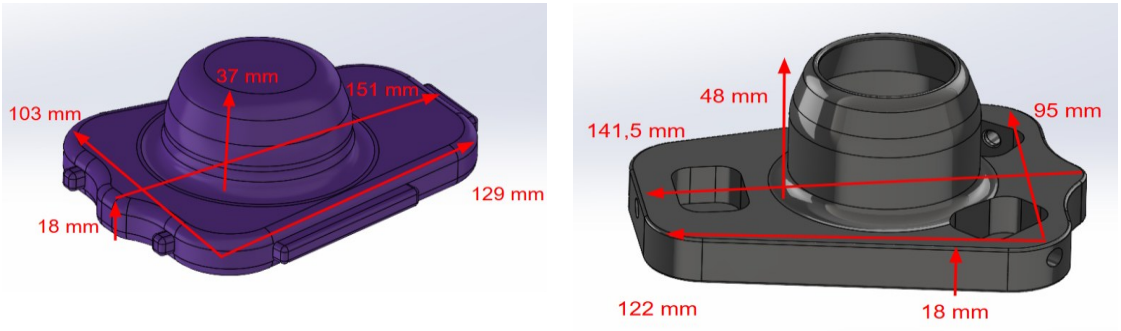

a) protrusion b) recess

Figure 9 Tongue-and-groove geometry

The design of the post-tensioning guide ducts incorporated a centring system to ensure the correct position of the bars during installation. For post-tensioning, high-strength Y1050 bars were selected, with a 26.5 mm diameter bar providing a nominal cross-sectional area (A) of 551 mm². This bar grade offers a characteristic yield strength ($f_{p0,1k}$) of 950 N/mm² and a tensile strength (f_{pk}) of 1,050 N/mm². The mechanical capacity of the selected diameter exhibits a yield load ($F_{p0,1k}$) of 525 kN and an ultimate breaking load (F_{pk}) of 580 kN per bar. These high-performance characteristics ensure that the required compressive stress is maintained across the segments, making the 3D-printed modular system into a monolithic structural element.

3.2.3 Lifting and Handling Systems

Given the production procedure of the segments, those required specific elements for lifting and handling operations. Since the elements were printed following a vertical direction, these had to be rotated 90 degrees to their final assembly position. Accordingly, temporary T-shaped steel anchorages were installed at the edges of each segment, those oriented for lifting operations. For segment rotation, eyebolts, in combination with HEB100 profiles, were installed for providing additional supports. Figure 10 shows both types of anchorages installed at each segment.

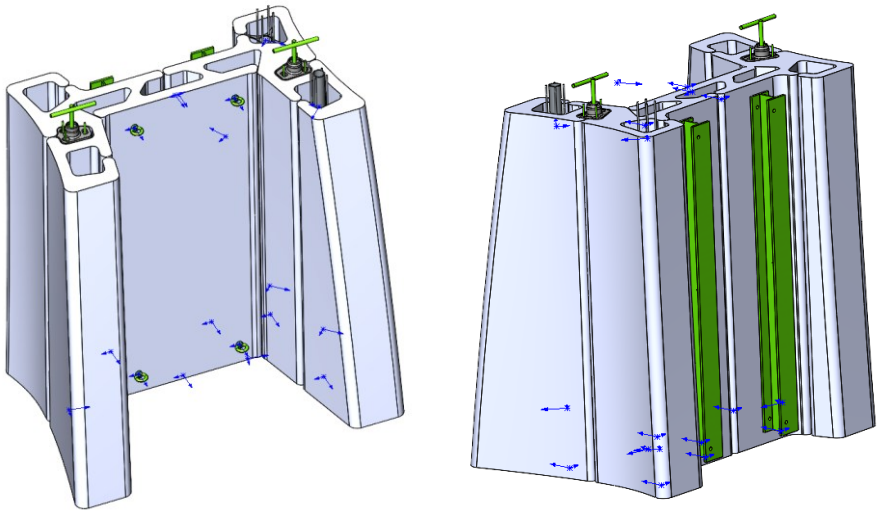

Figure 10 Handling and lifting anchorages and steel profiles

3.2.4 T-elements Design and Steel-to-Mortar Bond

The T-elements consist of anchoring points embedded in the segment voids where the tongue-and-groove elements are placed. In this case, steel rebars were placed along the full length of the segment void, finishing with a T-shaped geometry for lifting operations. A schematic representation of the T-elements along with the forces is presented in Figure 11.

Following *Eurocode 2* (EN 1992-1-1:2004), as a reference even though the cement-based material used for the production was rather a mortar, the axial force of a corrugated steel bar depends on the ultimate bond stress (f_{bd}), determined as specified in Eq. 1. For this, it was considered a mortar with a compressive strength of 19.30 MPa and a design tensile strength (f_{ctd}) of 1.50 MPa, the coefficient η_1 = 0.70 (poor bond conditions), and the coefficient η_2 established at 1.0 given that the

 https://doi.org/10.59238/j.pt.20260429001

diameter of the bar used (ϕ = 16 mm) is below 32 mm, thus obtaining a bond stress of 2.4 MPa.

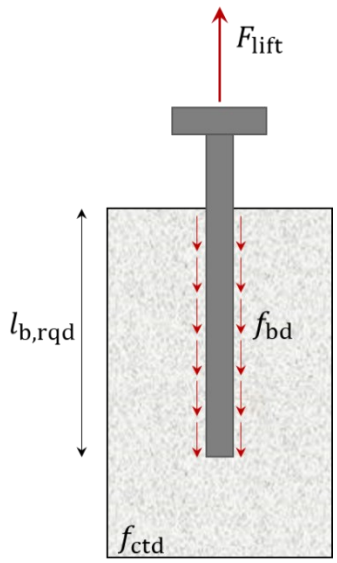

Figure 11 Schematic representation of stee-to-mortar bond forces

$$f_{\text{bd}} = 2.25 \cdot \eta_1 \cdot \eta_2 \cdot f_{\text{ctd}} \tag{1}$$

The minimum required anchorage length ($l_{\text{b,rqd}}$) was determined to be 124 mm, based on Eq 2. For this, the working stress in the bar (σ_{sd}) was determined considering the most unfavourable loading scenario (73.37 MPa), where the stress is evaluated over the net area of a 16 mm diameter bar (ϕ) under the lifting load while considering failure of one of the lifting bars and, hence, only one bar resisting the weight of the segment. Given that the actual embedded length is 1500 mm, the system achieves an exceptional margin of safety (MoS) of 24.0 against pull-out failure.

$$l_{b,rqd} = \frac{\phi}{4} \cdot \frac{\sigma_{sd}}{f_{bd}} \tag{2}$$

Subsequently, the margin of safety for the tensile stresses of the steel was verified according with Eq. 3 to ensure the bars operate well within their elastic limit (σ_{yield} = 400 MPa). For a total load of 14.8 kN distributed across 2 anchoring points, the resulting margin is 10.9, confirming a robust redundant design.

$$MoS_{rebar} = \frac{A_S \cdot \sigma_{yield} \cdot N}{P \cdot G} \tag{3}$$

3.2.5 Cold Joint Resistance

As this specific interface is not explicitly covered by current standards, a geometric progression (Figure 12) model was proposed to provide a more realistic estimation of the stress distribution. Unlike linear models that assume uniform shear, this analytical approach assumes that the load transfer is concentrated in the initial layers of the joint. Eq. 4 describes the load carried by a specific layer (P_i), the total load (P_{tot}), a distribution factor (r = 0.95), which indicates that each layer supports 5% less load than the previous layer, and the active layers (n = 30), which indicates the assumed number of layers that carry the load before stress dissipation.

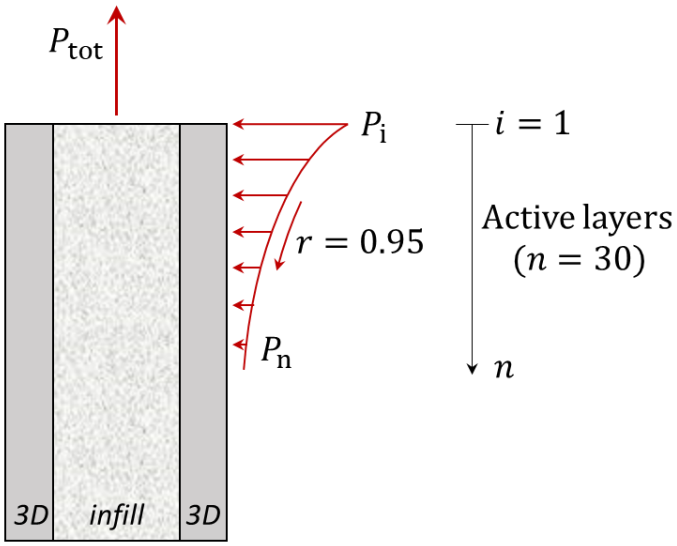

Figure 12 Geometric progression of stress distribution

$$P_i = P_{tot} \cdot \frac{(1-r) \cdot r^{(i-1)}}{1-r^n} \tag{4}$$

Based on these calculations, the load on the most critical first layer was estimated at 939 N, which leads to a margin of safety of 4.8 under distribution. This analytical approach confirms that the anchorage remains safe even when accounting for the complex mechanical interaction between the cast-in-place infill and the 3D-printed mortar.

3.2.6 Eyebolt Dimensioning

To ensure structural integrity during the 90-degree rotation (Figure 13), the eyebolts were dimensioned using an analytical approach. Given the brittle nature of unreinforced 3D-printed mortar and the dynamic effects of crane manipulation, the safety margin for the eyebolts was calculated using the mechanical equilibrium as described in Eq 5.

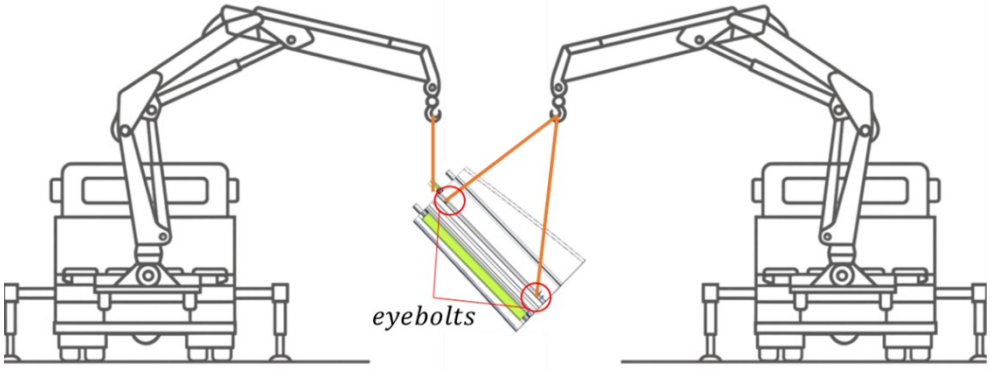

Figure 13 Lifting operation and positioning of eyebolts

$$MoS_{eyebolts} = \frac{S_{eqM12} \cdot \sigma_e \cdot N}{P \cdot G} \tag{5}$$

The calculation used four lifting points (N = 4) with grade 8.8 steel rods, characterized by a yield strength (σ_e) of 640 MPa and an effective stress area (S_{eq}) of 84.30 mm². These parameters were evaluated considering the most unfavourable loading scenario, this being the maximum segment weight (P) of 12.9 kN and the

 https://doi.org/10.59238/j.pt.20260429001

gravitational acceleration (G) 9.81 m/s². By applying these values to Eq. 5, a margin of safety of 14.6 was obtained.

The margin of safety achieved significantly exceeds standard industrial lifting requirements (which typically range between 4 and 6). Such over-dimensioning of the eyebolts was considered for security reasons given the necessity of taking into consideration that during lifting and rotation operations, segments are subjected to inertial forces and potential shocks. Additionally, the calculation assumes a perfectly balanced load though, in real conditions, lifting and rotational operations may lead to uneven load distributions among the lifting points.

4 Construction Processes

4.1 3D Printing and Manufacturing of Segments

After conducting the printing simulations and validating the operational manufacturing aspects, the segments were produced. During production (Figure 14), printing and operational parameters were recorded for repeatability purposes, and the material behaviour was controlled taking special attention to material deposition, geometrical continuity at critical zones and layer height, width, and stability. However, and despite this controlled environment, variations in material consistency at the extrusion point represented one the major challenges given the sensitivity of the pumping system to temperature and humidity. Accordingly, structural stability took great relevance given the height of the elements, since material performance needed to achieve a minimum strength to support the increasing pressure of the upper layers to avoid local buckling.

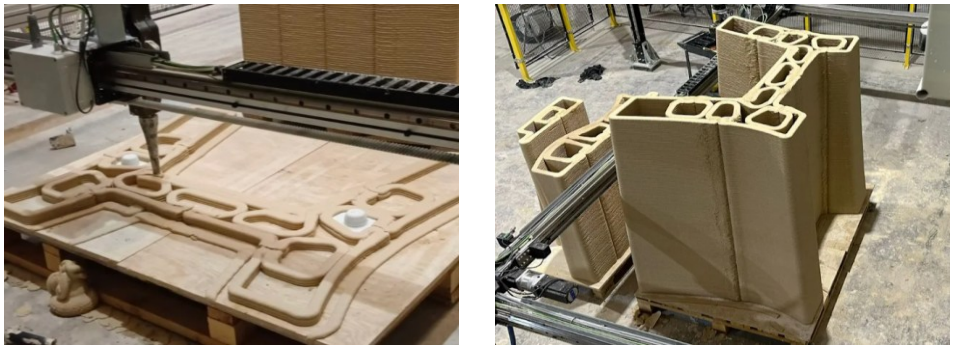

Figure 14 Printing procedure of the segments

Lifting and handling systems as well as the post-tensioning elements were integrated into the segments during production (Figure 15). Recess tongue-and-groove elements were placed at the bottom edge of the segment at the beginning of the printing process, whereas protrusion elements were placed at the top after printing the whole element. T-shaped bars for lifting were inserted at the protrusion elements, filling with mortar the void of the segment for ensuring the bar anchorage. Figure 14 shows both the filling of the void and the insertion of the T-shaped bar. The internal ducts for the post-tensioning bars were also placed with guiding systems to guarantee the correct position within the voids of the segment.

Figure 15 Insertion of T-elements and ducts

After printing and installing the lifting and handling systems and the post-tensioning elements, post-processing operations and surface finish reviews were conducted to verify the integrity of the manufactured segments. These verifications confirmed the absence of relevant defects such as premature cracking, interlayer delamination, or local buckling, this validating the production process according with the designed geometry.

4.2 Logistics and Assembly: Transport, Orientation and Site Erection

The segments, once printed at the manufacturing facilities, were transported to worksite. To ensure structural integrity during handling, all assembly operations were conducted after 28 days to ensure that the mechanical properties of the material reached their required performance levels. At worksite, the segments were unloaded and subjected to a visual inspection, performed to detect any surface defects or micro-cracking that might have occurred by vibrations or stresses during transport.

Given that the modules were produced vertically during 3D printing, a tandem lifting and rotation strategy was performed using two mobile cranes to reorient the segments from the vertical printing orientation to the horizontal service position. For this, and while the segment remained at vertical position after unloading, two HEB 100 steel profiles were temporarily placed on what would become the bottom face of the module. These steel profiles were placed by drilling the segments and placing the high-strength bolts, fastening the modules to the steel profiles to provide the lifting points for the cranes (Figure 16). For the rotation of the elements, the main crane held the element vertically, while the auxiliary crane connected to the bolts of the HEB profiles rotated the segment into its horizontal final position, as shown in Figure 16.

Figure 16 Reorientation procedure

The connection between the 3D-printed concrete sections used the tongue-and-groove elements integrated into the segment faces to ensure the alignment of the modules during placement. Once placed, guide cords were inserted through the internal post-tensioning ducts to facilitate the subsequent placement of the post-tensioning steel bars. Once all modules were positioned (Figure 17), the footbridge was supported at three specific zones: the permanent end abutment and a central set of two provisional supports. These auxiliary supports were essential for sustaining the self-weight during this phase, as the bridge only achieves its self-supporting and monolithic behaviour once the post-tensioning force is applied.

Figure 17 Positioning of the segments and site erection

https://doi.org/10.59238/j.pt.20260429001

4.3 Post-Tensioning Operation and Load Transfer

After positioning and alignment of the four segments, high-strength steel bars were introduced through the internal ducts. For the tensioning, a hydraulic jack as displayed in Figure 18 was placed at the anchoring points at the edge of the structure. Given that a single hydraulic jack was used for the operation, it was necessary to follow a sequential tensioning procedure (Figure 18) given the necessity of providing a gradual and balanced increase in stress, preventing the introduction of undesired eccentricities or asymmetrical forces that could compromise the integrity of the segments. The loading strategy was defined by applying a pressure of 20 bar individually to each of the four bars, resulting in an effective axial force of 25 kN per bar, thus reaching a total compression force of 100 kN.

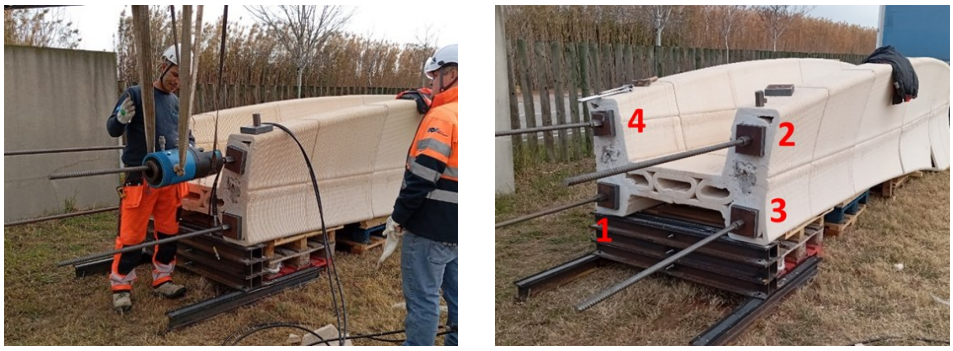

Figure 18 Post-tensioning procedure and sequential tensioning

After post-tensioning, the structure achieved a self-supporting condition and its definitive structural scheme without requiring the provisional supports. For the removal of the central set of provisional supports, the hydraulic jack used for post-tensioning was strategically repositioned at one of the edges of the footbridge to vertically lift the structure (Figure 19). Once the load on the temporary supports was released, those were removed and the footbridge was finally lowered onto its permanent support. This support consisted of a system of four HEB 100 steel profiles placed at the elevated end, finally consolidating the footbridge as a stable, simply supported beam.

Figure 19 Lifting of the footbridge for support positioning

5 Results and Conclusions

The design and manufacturing of the Goliath footbridge confirmed the technical feasibility of integrating topology optimization with 3D concrete printing and post-tensioning. The structural activation of the full footbridge reached a total compression of 100 kN, verifying the possibility of assembly different segments into a monolithic and self-supporting system. This process demonstrated that the structure is capable of sustaining its own weight and load transfer without the need for conventional continuous reinforcement across the joints. Additionally, the use of

dry-joint strategy with polymeric shear keys allowed the assembly of the elements, requiring only temporary supports before the final post-tensioning stage.

However, several technical challenges arised that should be taken into consideration for future industrial applications. The transition from digital models to physical reality revealed a significant sensitivity to dimensional tolerances. Moreover, even though the global structural performance was satisfactory, local fragility was observed in regions with high stress concentrations, such as geometry transitions and areas adjacent to the segment interfaces.

Experimental evidence during assembly and post-tensioning highlighted the susceptibility of printing layers and joint intersections. Specific areas exhibited local cracking that did not compromise the global stability of the structure, this introduced uncertainty regarding long-term durability and fatigue resistance. These cracks confirm that 3D-printed mortar without conventional (or fibre) reinforcement is highly sensitive to stresses concentration, which are often difficult to capture accurately in numerical models. Therefore, the implementation of this technology at a larger scale will necessarily require advanced material reinforcement strategies.

Based on these findings, essential recommendations have been identified as key aspects for future research and industrial production:

- The incorporation of structural fibres (metallic or synthetic) is recommended to improve post-cracking strength, control crack widths, and reduce local fragility.
- Design should avoid sharp corners and introduce reinforced anchorage zones to better distribute post-tensioning loads.
- Inspection of internal duct placement and interlayer bond strength should be integrated into the manufacturing procedure verification before structural assembly.
- Analysis and study of new hybrid joint solutions that may combine dry mechanical interlock with localized high-strength grouting to enhance environmental protection of the post-tensioning system to improve durability.

Conflict of Interest Statement: The authors declare that there is no conflict of interest regarding the publication of this paper.

Funding: This publication is part of the R&D project PLEC2022-009441, funded by MICIU/AEI/10.13039/501100011033 and by the European Union NextGenerationEU/PRTR. CIM-UPC and Lagula Arquitectes were partners of the project and their contributions in the design and technical development were essential. Additionally, the authors acknowledge Aridditive for their support in the manufacturing of the 3D-printed segments.

References

1. Asprone, D.; Auricchio, F.; Menna, C.; Mercuri, V. 3D printing of reinforced concrete elements: Technology and design approach. *Construction and Building Materials* **2018**, *165*, 218-231, doi:10.1016/j.conbuildmat.2018.01.018.
2. Cabibihan, J.-J.; Gaballa, A.; Fadli, F.; Irshidat, M.; Mahdi, E.; Biloria, N.; Mansour, Z.; Abdulrazak, H. A guided approach for utilizing concrete robotic 3D printing for the architecture, engineering, and construction industry. *Construction Robotics* **2023**, *7*, 265-278, doi:10.1007/s41693-023-00103-9.
3. Menna, C.; Mata-Falcón, J.; Bos, F.P.; Vantyghem, G.; Ferrara, L.; Asprone, D.; Salet, T.; Kaufmann, W. Opportunities and challenges for structural engineering of digitally fabricated concrete. *Cement and Concrete Research* **2020**, *133*, doi:10.1016/j.cemconres.2020.106079.

4. Asensio, J.; Josa, I.; Monserrat, A.; de la Fuente, A. 3D‐printed concrete footbridges: An approach to assess the sustainability performance. *Structural Concrete* **2023**, *24*, 7705-7725, doi:10.1002/suco.202201227.
5. Zhang, Y.; de Lima, L.N.; Böhler, D.; Arunothayan, A.; Babafemi, A.J.; Baz, B.; Caneda-Martinez, L.; De Schutter, G.; Du, H.; Freund, N.; et al. Durability assessment of 3D printed cement-based materials: a RILEM TC 304-ADC interlaboratory study. *Materials and Structures* **2025**, *58*, doi:10.1617/s11527-025-02797-5.
6. Mechtcherine, V.; Muthukrishnan, S.; Robens-Radermacher, A.; Wolfs, R.; Versteege, J.; Menna, C.; Ozturk, O.; Ozyurt, N.; Roupec, J.; Richter, C.; et al. Mechanical properties of 3D printed concrete: a RILEM 304-ADC interlaboratory study – compressive strength and modulus of elasticity. *Materials and Structures* **2025**, *58*, doi:10.1617/s11527-025-02688-9.
7. Robens-Radermacher, A.; Kujath, C.; Bos, F.; Mechtcherine, V.; Unger, J.F. Mechanical properties of 3D printed concrete: a RILEM TC 304-ADC interlaboratory study-Design and implementation of a database system for querying, sharing, and analyzing experimental data. *Materials and Structures* **2025**, *58*, doi:10.1617/s11527-025-02650-9.
8. Wolfs, R.; Versteege, J.; Santhanam, M.; Bhattacherjee, S.; Bos, F.; Robens-Radermacher, A.; Muthukrishnan, S.; Menna, C.; Ozturk, O.; Ozyurt, N.; et al. Mechanical properties of 3D printed concrete: a RILEM TC 304-ADC interlaboratory study — flexural and tensile strength. *Materials and Structures* **2025**, *58*, doi:10.1617/s11527-025-02687-w.
9. Bos, F.; Menna, C.; Robens-Radermacher, A.; Wolfs, R.; Roussel, N.; Lombois-Burger, H.; Baz, B.; Weger, D.; Nematollahi, B.; Santhanam, M.; et al. Mechanical properties of 3D printed concrete: a RILEM TC 304-ADC interlaboratory study — approach and main results. *Materials and Structures* **2025**, *58*, doi:10.1617/s11527-025-02686-x.
10. Zhang, X.; Li, M.; Lim, J.H.; Weng, Y.; Tay, Y.W.D.; Pham, H.; Pham, Q.-C. Large-scale 3D printing by a team of mobile robots. *Automation in Construction* **2018**, *95*, 98-106, doi:10.1016/j.autcon.2018.08.004.
11. Zuo, Z.; De Corte, W.; Huang, Y.; Chen, X.; Zhang, Y.; Li, J.; Zhang, L.; Xiao, J.; Yuan, Y.; Zhang, K.; et al. Strategies towards large-scale 3D printing without size constraints. *Virtual and Physical Prototyping* **2024**, *19*, doi:10.1080/17452759.2024.2346821.
12. Miri, Z.S.; Baaj, H.; Polak, M.A. 3D-Printed Concrete Bridges: Material, Design, Construction, and Reinforcement. *Applied Sciences* **2025**, *15*, doi:10.3390/app15063054.
13. Mitrović, S.; Ignjatović, I. Experimental investigation of bearing capacity of 3D printed concrete segmental girder. *Gradjevinski materijali i konstrukcije* **2024**, *67*, 137-146, doi:10.5937/grmk2400008m.
14. Cai, J.; Wang, J.; Zhang, Q.; Du, C.; Meloni, M.; Feng, J. State-of-the-art of mechanical properties of 3D printed concrete. *Case Studies in Construction Materials* **2024**, *21*, doi:10.1016/j.cscm.2024.e03847.
15. Salet, T.A.M.; Ahmed, Z.Y.; Bos, F.P.; Laagland, H.L.M. Design of a 3D printed concrete bridge by testing. *Virtual and Physical Prototyping* **2018**, *13*, 222-236, doi:10.1080/17452759.2018.1476064.
16. Gebhard, L.; Mata-Falcón, J.; Anton, A.; Dillenburger, B.; Kaufmann, W. Structural behaviour of 3D printed concrete beams with various reinforcement strategies. *Engineering Structures* **2021**, *240*, doi:10.1016/j.engstruct.2021.112380.
17. Lowke, D.; Dini, E.; Perrot, A.; Weger, D.; Gehlen, C.; Dillenburger, B. Particle-bed 3D printing in concrete construction – Possibilities and challenges. *Cement and Concrete Research* **2018**, *112*, 50-65, doi:10.1016/j.cemconres.2018.05.018.
18. de la Fuente, A.; Blanco, A.; Galeote, E.; Cavalaro, S. Structural fibre-reinforced cement-based composite designed for particle bed 3D printing systems. Case study Parque de Castilla Footbridge in Madrid. *Cement and Concrete Research* **2022**, *157*, doi:10.1016/j.cemconres.2022.106801.
19. Xu, W.; Gao, Y.; Sun, C.; Wang, Z.H.I. Fabrication and Application of 3d-Printed Concrete Structural Components in the Baoshan Pedestrian Bridge Project. In *Fabricate 2020*; 2020; pp. 140-147.
20. Vantyghem, G.; De Corte, W.; Shakour, E.; Amir, O. 3D printing of a post-tensioned concrete girder designed by topology optimization. *Automation in Construction* **2020**, *112*, doi:10.1016/j.autcon.2020.103084.
21. Kinomura, K.; Murata, S.; Yamamoto, Y.; Obi, H.; Hata, A. Application of 3D Printed Segments Designed by Topology Optimization Analysis to a Practical Scale Prestressed Pedestrian Bridge. In *Second RILEM International Conference on Concrete and Digital Fabrication*; RILEM Bookseries; 2020; pp. 658-668.
22. Ahmed, Z.; Wolfs, R.; Bos, F.; Salet, T. A Framework for Large-Scale Structural Applications of 3D Printed Concrete: the Case of a 29 m Bridge in the Netherlands. *Open Conference Proceedings* **2022**, *1*, 5-19, doi:10.52825/ocp.v1i.74.
23. Dell'Endice, A.; Bouten, S.; Van Mele, T.; Block, P. Structural design and engineering of Striatus, an unreinforced 3D-concrete-printed masonry arch bridge. *Engineering Structures* **2023**, *292*, doi:10.1016/j.engstruct.2023.116534.
24. Bhooshan, S.; Bhooshan, V.; Dell'Endice, A.; Chu, J.; Singer, P.; Megens, J.; Van Mele, T.; Block, P. The Striatus bridge. *Architecture, Structures and Construction* **2022**, *2*, 521-543, doi:10.1007/s44150-022-00051-y.
25. Ooms, T.; Vantyghem, G.; Tao, Y.; Bekaert, M.; De Schutter, G.; Van Tittelboom, K.; De Corte, W. The Production of a Topology-Optimized 3D-Printed Concrete Bridge. In *Third RILEM International Conference on Concrete and Digital Fabrication*; RILEM Bookseries; 2022; pp. 37-42.
26. Pons-Valladares, O.; Casanovas-Rubio, M.d.M.; Armengou, J.; de la Fuente, A. Approach for sustainability assessment for footbridge construction technologies: Application to the first world D-shape 3D-Printed fiber-reinforced mortar footbridge in Madrid. *Journal of Cleaner Production* **2023**, *394*, doi:10.1016/j.jclepro.2023.136369.

27. Talebi, S.; Koskela, L.; Tzortzopoulos, P.; Kagioglou, M. Tolerance Management in Construction: A Conceptual Framework. *Sustainability* **2020**, *12*, doi:10.3390/su12031039.
28. Enshassi, M.S.A.; Walbridge, S.; West, J.S.; Haas, C.T. Integrated Risk Management Framework for Tolerance-Based Mitigation Strategy Decision Support in Modular Construction Projects. *Journal of Management in Engineering* **2019**, *35*, doi:10.1061/(asce)me.1943-5479.0000698.
29. Arashpour, M.; Heidarpour, A.; Akbar Nezhad, A.; Hosseinifard, Z.; Chileshe, N.; Hosseini, R. Performance-based control of variability and tolerance in off-site manufacture and assembly: optimization of penalty on poor production quality. *Construction Management and Economics* **2019**, *38*, 502-514, doi:10.1080/01446193.2019.1616789.
30. Shi, A.; Lee, K.L.; Bo, S.; Koh, W.K.; Jun, D.P.W.; Wong, S.F.; Chen, H.; Lin, A. Dimensional Effects on Shear Behaviour of 3D-Printed Concrete Shear Keys. In *Proceedings of the First International Conference on Engineering Structures*; Lecture Notes in Civil Engineering; 2025; pp. 557-566.
31. Rausch, C.; Lu, R.; Talebi, S.; Haas, C. Deploying 3D scanning based geometric digital twins during fabrication and assembly in offsite manufacturing. *International Journal of Construction Management* **2021**, *23*, 565-578, doi:10.1080/15623599.2021.1896942.
32. İlcan, H.; Külak, A.Y.; Şahin, O.; Aldemir, A.; Şahmaran, M.; Lachemi, M. Reinforcement and modular system for 3DCP geopolymer structures using construction and demolition waste. *Construction and Building Materials* **2025**, *474*, doi:10.1016/j.conbuildmat.2025.141115.
33. Sørensen, J.H.; Herfelt, M.A.; Hoang, L.C.; Muttoni, A. Test and lower bound modeling of keyed shear connections in RC shear walls. *Engineering Structures* **2018**, *155*, 115-126, doi:10.1016/j.engstruct.2017.11.004.
34. Feng, J.; Liang, W.; Jiang, H.; Huang, C.; Zhang, J. Shear performance of single-keyed dry joints between reactive power concrete and high strength concrete in push-off tests. *Science Progress* **2020**, *103*, doi:10.1177/0036850420928643.
35. Pan, R.; He, W.; Cheng, L.; Li, C. Direct Shear Strength of UHPC Large-Keyed Epoxy Joint: Theoretical Model and Experimental Verification. *Journal of Bridge Engineering* **2022**, *27*, doi:10.1061/(asce)be.1943-5592.0001936.
36. Wang, L.; Liu, Y.; Yang, Y.; Li, Y.; Bai, M. Bonding performance of 3D printing concrete with self-locking interfaces exposed to compression–shear and compression–splitting stresses. *Additive Manufacturing* **2021**, *42*, doi:10.1016/j.addma.2021.101992.
37. Hua, T.; Lin, A.; Poh, W.J.D.; Charlene; Wong, D.H.A.; Zhang, H.; Chan, Y.Z.; Liu, W.; Zhao, L. 3D-printed concrete shear keys: Design and experimental study. *Developments in the Built Environment* **2023**, *15*, doi:10.1016/j.dibe.2023.100180.
38. Assaad, J.J.; Abou Yassin, A.; Alsakka, F.; Hamzeh, F. A Modular Approach for Steel Reinforcing of 3D Printed Concrete—Preliminary Study. *Sustainability* **2020**, *12*, doi:10.3390/su12104062.
39. Saibabu, S.; Srinivas, V.; Sasmal, S.; Lakshmanan, N.; Iyer, N.R. Performance evaluation of dry and epoxy jointed segmental prestressed box girders under monotonic and cyclic loading. *Construction and Building Materials* **2013**, *38*, 931-940, doi:10.1016/j.conbuildmat.2012.09.068.
40. Zou, Y.; Xu, D. Experimental study on shear behavior of joints in precast concrete segmental bridges. *Structures* **2022**, *39*, 323-336, doi:10.1016/j.istruc.2022.03.037.
41. Zou, Y.; Xu, D. Shear behavior of steel keyed joints in precast concrete segmental bridges under direct shear loading. *Structural Concrete* **2022**, *23*, 2710-2731, doi:10.1002/suco.202100422.
42. Yu, J.; Xia, Y.; Zhang, G.; Jiang, C. Shear strength of reactive powder concrete dry joints in prefabricated buildings. *Structures* **2025**, *78*, doi:10.1016/j.istruc.2025.109278.
43. Li, Y.; Wang, R.; Ma, Y.; Zhao, G.; Wang, S.; Lv, J.; Ye, B. Direct shear behavior of steel fiber-reinforced concrete single-keyed dry joints: Finite element analysis and calculation model. *Structures* **2025**, *81*, doi:10.1016/j.istruc.2025.110362.
44. Cui, W.; Guo, R.; Liu, W.; Wan, D.; Shi, X.; Sun, Y.; Gong, J.; Tao, Y. Quality assessment of 3D‐printed concrete through quantitative visual inspection. *Structural Concrete* **2025**, *26*, 8292-8306, doi:10.1002/suco.70235.
45. Cui, W.; Liu, W.; Guo, R.; Wan, D.; Yu, X.; Ding, L.; Tao, Y. Geometrical quality inspection in 3D concrete printing using AI-assisted computer vision. *Materials and Structures* **2025**, *58*, doi:10.1617/s11527-025-02594-0.
46. Buswell, R.; Xu, J.; De Becker, D.; Dobrzanski, J.; Provis, J.; Kolawole, J.T.; Kinnell, P. Geometric quality assurance for 3D concrete printing and hybrid construction manufacturing using a standardised test part for benchmarking capability. *Cement and Concrete Research* **2022**, *156*, doi:10.1016/j.cemconres.2022.106773.
47. AENOR (Asociación Española de Normalización y Certificación). EN 12390-3 Testing hardened concrete. Part 3: Compressive strength of test specimens. 2019.
48. Dassault Systèmes. Simulia Dassault Systèmes. Abaqus CAE user's manual. **2012**.
49. Chisari, C.; Amadio, C. TOSCA: a Tool for Optimisation in Structural and Civil engineering Analyses. *International Journal of Advanced Structural Engineering* **2018**, *10*, 401-419, doi:10.1007/s40091-018-0205-1.

AUTHOR BIOGRAPHIES

<table>
<tr>
<td>  </td>
<td>Albert de la Fuente
Full Professor at the Department of Civil and Environmental Engineering, Universitat Politècnica de Catalunya (UPC BarcelonaTech).
Research Direction: Fibre reinforced concrete, structural design and assessment, low-carbon cement-based materials, circular construction, 3D printed concrete structures, digitalization and smart monitoring of infrastructures, and life-cycle sustainability assessment of concrete structures and infrastructures.
Email: albert.de.la.fuente@upc.edu</td>
<td>  </td>
<td>Eduardo Galeote
Assistant Professor at the Department of Architectural Technology, Universitat Politècnica de Catalunya (UPC BarcelonaTech).
Research Direction: Fibre reinforced concrete, the experimental and numerical study of cement-based materials, structural applications and quality control, the design and development of innovative testing methods, special concretes, digital fabrication, 3D printing concrete and sustainable materials for the construction industry.
Email: eduardo.galeote@upc.edu</td>
</tr>
<tr>
<td>  </td>
<td>Alejandro Nogales
Senior researcher at Smart Engineering (spin-off UPC).
Research Direction: Fibre reinforced concrete structures, non-linear finite element modelling, flat slabs and tunnel segments, serviceability and crack control design, structural optimization, recycled aggregate concrete systems, and the experimental and numerical assessment of innovative concrete elements for sustainable construction.
Email: alejandro.nogales@upc.edu</td>
<td>  </td>
<td>Ye Xia
D.Eng, P.E., Associate professor at Department of Bridge Engineering, Tongji University.
Research Direction: Bridge health monitoring, structural intelligent assessment, big data fusion analysis, image recognition technology, machine learning and deep learning.

Email: yxia@tongji.edu.cn</td>
</tr>
<tr>
<td> 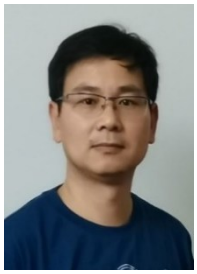 </td>
<td>Fangyuan Li
D. Eng, Professor, Department of Bridge Engineering, Tongji University.
Research Direction: Bridge engineering, 3D Print and new material new technology.

Email: fyli@tongji.edu.cn</td>
<td></td>
<td></td>
</tr>
</table>